# Electron transport in the $Hg_{1-x}Cd_xSe$ alloy system

D. A. Nelson,* J. G. Broerman, C. J. Summers, and C. R. Whitsett
*McDonnell Douglas Research Laboratories, McDonnell Douglas Corporation, Saint Louis, Missouri 63166*
(Received 21 February 1978)

An experimental and theoretical study of the electron mobility in the semimetal-semiconductor alloy system $Hg_{1-x}Cd_xSe$ is reported for the range of compositions $0.12 \leq x \leq 0.68$ and at temperatures from 4.2 to 300 K. The samples used in the study are single-crystal specimens grown by the traveling-molten-zone and the Bridgman methods. The mobility data are analyzed in terms of a microscopic theory of electrical conduction appropriate to the alloy system, and the dominant intrinsic and defect-scattering mechanisms are determined. The analysis includes scattering of electrons by longitudinal-optical phonons, longitudinal- and transverse-acoustical phonons, charged and neutral defects, heavy holes, and the compositional disorder potential of the alloy. It is found that longitudinal-optical-phonon scattering is the dominant mechanism at room temperature for all alloys in the composition range studied. Acoustical-phonon scattering is unimportant at all temperatures and compositions. Scattering associated with the compositional disorder of the alloy increases from 5% of the total scattering at $x = 0.12$ to 21% at $x = 0.68$. Evidence is presented for the presence of four defect species: a donor associated with the HgSe lattice, a donor associated with the CdSe lattice, an acceptor associated with the CdSe lattice, and a stable neutral defect associated with the HgSe lattice.

## I. INTRODUCTION

Mercury selenide (HgSe) is a perfect semimetal,[1-4] having a symmetry-induced degeneracy of the valence-band maximum and conduction-band minimum which produces an identically-zero fundamental direct energy gap. Cadmium selenide (CdSe) is a semiconductor with a fundamental direct gap of 1.8 eV.[5] These compounds combine in a pseudobinary alloy system, $Hg_{1-x}Cd_xSe$, and the alloy energy gap ranges from 0 to 1.8 eV depending on composition. The energy-band structures of the compounds and the alloys are shown in Fig. 1. In HgSe the $\Gamma_6$ level, which in a normal semiconductor is the extremum of a conduction band, lies below the fourfold-degenerate $\Gamma_8$ level, which is normally the edge of the light- and heavy-hole valence bands. The light-hole part of $\Gamma_8$, being $\vec{k}\cdot\vec{p}$ coupled to $\Gamma_6$, inverts to form a small-mass conduction band, and the $\Gamma_6$ level becomes a valence band lying between the split-off band ($\Gamma_7$) and the heavy-hole band. Since the $\Gamma_8$ conduction band is tied to the $\Gamma_8$ valence band by symmetry, the gap is identically zero. As CdSe is added, the virtual crystal $\Gamma_6$ level rises with respect to the $\Gamma_8$ level and crosses it at about $x=0.1$. Above this critical value of $x$, the alloy is a normal InSb-type semiconductor with a direct energy gap, which depends on the composition. In this discussion and in Fig. 1, we ignore the existence of a structural phase transformation from zinc blende (HgSe) to wurtzite (CdSe) and use throughout the zinc-blende symmetry nomenclature.

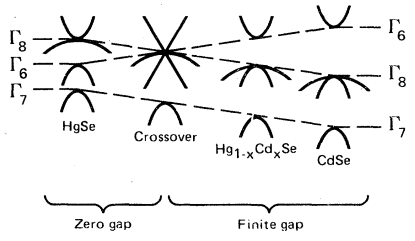


FIG. 1. Band structures of HgSe, CdSe, and the $Hg_{1-x}Cd_xSe$ alloys. The mole fraction of CdSe, $x$, increases toward the right. The characteristics of the alloy change from semimetallic (HgSe) to semiconducting (CdSe) with increasing $x$, as the virtual crystal $\Gamma_6$ level rises with respect to the $\Gamma_8$ level and a gap in the density of states begins to open at the crossover composition.

In the original crystallographic investigation of $Hg_{1-x}Cd_xSe$, Kalb and Leute[6] reported that the alloys with $x \leq 0.77$ have the zinc-blende structure, alloys with $x \geq 0.81$ have the wurtzite structure, and the two phases are immiscible for $0.77 < x < 0.81$. Their data were for sintered samples, equilibrated at temperatures substantially less than the melting point of the alloy. More recently, an investigation[7] of the phase diagram for this alloy system showed that a peritectic reaction occurs at 945 °C and that upon solidification from the melt, alloys with $x < 0.57$ have the zinc-blende crystal structure while alloys with $x > 0.57$ have the wurtzite structure.

A number of investigations of the galvanomagnetic and optical properties of the alloy system have been performed. Stankiewicz, Giriat, and Dobrowski[8] studied the Shubnikov–de Haas effect for alloys with $x < 0.2$ and determined the conduction-band effective mass as a function of alloy composition. Optical studies have been performed by

Borisov, Kiriev, Mikhailin, and Bezborodova,[9] by Kiriev and Volkov,[10] and by Slodowy and Giriat.[11] The investigation by Borisov *et al.* concerned primarily the higher-energy optical transitions, and their analysis gave a composition independent band gap because of an incorrect identification of reflectivity structure. More recently, detailed investigations of the optical absorption[12] and relectance[13] have determined the band gap as a function of temperature for a wide range of compositions ($0.1 < x < 0.7$) and the lattice-dynamic and electronic polarizability properties of the alloys. These results provide the basis for a detailed microscopic analysis of the electrical transport properties of the system.

The electrical transport properties of the $Hg_{1-x}Cd_xSe$ alloys have been little studied. A qualitative description was given by Cruceanu and Ionescu-Bujor.[14] Iwanowski and Dietl[15] investigated the 4.2-K electron mobility of alloys with $0 < x \leq 0.2$, and they noted discrepancies between the measured values and those calculated assuming ionized defect scattering only. In both of the cited investigations, the alloys were reported to have $n$-type conductivity, as do HgSe and CdSe. An adequate understanding of the electrical transport properties of this system requires data and analysis over larger ranges of composition and temperature than have been studied.

In this paper, we report an experimental and theoretical investigation of the electron mobility in $Hg_{1-x}Cd_xSe$ alloys with $0.12 \leq x \leq 0.68$ for temperatures between 4.2 and 300 K. The preparation of samples and the methods of measuring the Hall coefficient and electrical conductivity are described in Sec. II. In Sec. III the experimental electron mobilities are analyzed in terms of a microscopic theory of electrical conduction, and the dominant intrinsic and extrinsic (defect) electron-scattering mechanisms are determined. The analysis assumes a virtual crystal band structure, with parameters given by the optical measurements of Ref. 12. The conduction-electron wave functions and dispersion relation are then described by the exact Kane three-band model.[16] Using this band model and the lattice dynamic and electronic polarizability parameters determined in Ref. 13, the Boltzmann equation for the electron distribution function is formulated. The scattering mechanisms included in the analysis are longitudinal-optical and acoustical-phonon scattering, charged and neutral defect scattering, electron-hole scattering, and scattering by the random compositional disorder potential of the alloy. The mobility is then calculated from a variational solution of the Boltzmann equation and compared with the experimental values. The results of the study are discussed in Sec. IV.

In this study, we are not concerned with the range of $x$ for which the alloy has the perfect semimetal band structure. A discussion of the unusual electronic transport and dielectric properties of the inverted band-structure is given in Ref. 4 and 17.

## II. SAMPLE PREPARATION AND CHARACTERIZATION

The samples used in this study were prepared from large single-crystal grains obtained from ingots grown by the Bridgman method[17] or the horizontal traveling molten zone method.[18] Sample composition and homogeneity were determined by mass density and scanning-infrared transmission measurements; the precision of the $x$ determination was estimated to be $\pm 0.003$, and the variation in $x$ within each sample did not exceed $\pm 0.002$. Most samples were circular wafers approximately 0.7 mm thick and 7 mm in diameter. Other samples were $1.5 \times 1.5 \times 10$ mm rectangular parallelipipeds.

The Hall coefficient and electrical conductivity of the samples were measured using low-frequency ac techniques with phase-sensitive detection; the Van der Pauw method[19] was used for the circular wafers and the conventional method was used for the rectangular parallelipiped samples. Identical results were obtained on samples in which both methods were used. Electrical leads were 0.05-mm-diam platinum wires, which were either welded to the samples or attached with silver paint to achieve ohmic electrical contacts. Before electrical leads were attached, the samples were ground, polished, and etched in a solution of 1-vol% $Br_2$ in methanol and repeatedly rinsed in a 50% ethonal, 50% benzene solution.

The electron concentration and mobility were calculated from the Hall coefficient and conductivity assuming a Hall scattering factor of unity. In many cases Shubnikov–de Haas oscillations were observed at low temperatures, and the electron concentrations deduced from the periods of these oscillations agreed with the Hall coefficient data to within 5%.

The $Hg_{1-x}Cd_xSe$ alloys were $n$-type with as-grown electron concentrations decreasing from $3 \times 10^{18}$ electrons/cm$^3$ for HgSe ($x = 0$) to as low as $1.3 \times 10^{16}$ electrons/cm$^3$ for alloys with $x > 0.4$. Annealing the alloys in Hg vapor increased the electron concentration, with the magnitude of the increase being smaller for alloys with larger $x$ values. Although the electron concentrations were reduced by annealing the alloy in Se vapor, the lowest electron concentrations were achieved by annealing the alloys in dynamic vacuum. The op-

timum annealing temperature for achieving the smallest electron concentrations in dynamic vacuum annealed alloys increases from 200°C for alloys with $x = 0.1$ to approximately 300°C for alloys with $x > 0.4$.

The conduction-electron concentration and electron mobility at 4.2, 78, and 300 K for samples investigated in this study are listed in Table I. Also listed in Table I are the specimen annealing histories and the mole fraction CdSe as determined

TABLE I. Electrical characteristics and annealing history of $Hg_{1-x}Cd_xSe$ samples.

| $Hg_{1-x}Cd_xSe$ Sample No. | Mole fraction of CdSe, $x$ | Conduction-electron concentration, $n$ ($10^{16}$ cm$^{-3}$) | | | Electron mobility, $\mu$ (cm$^2$/V sec) | | | Anneal history[a] |
|---|---|---|---|---|---|---|---|---|
| | | 4.2 K | 78 K | 300 K | 4.2 K | 78 K | 300 K | |
| 14AE-1 | 0.122 | 15.3 | 15.3 | 15.3 | 130 000 | 85 600 | 8690 | As grown |
| 14AE-2 | 0.122 | 7.03 | 7.17 | 10.8 | 277 000 | 177 000 | 9720 | VA—24 h at 200°C |
| 14AE-3 | 0.122 | 197.0 | 197.0 | 197.0 | 24 200 | 20 000 | 5530 | Hg—45 h at 225°C |
| 16EC8 | 0.153 | 2.94 | 2.94 | 5.37 | 271 000 | 114 000 | 6280 | VA—48 h at 239°C |
| 16EC12 | 0.153 | 5.65 | 5.71 | 7.55 | 157 000 | 86 700 | 7070 | VA—288 h at 203°C |
| 16DA1t | 0.162 | 16.2 | 17.2 | 19.4 | 141 000 | 84 100 | 8480 | As grown |
| 18MB | 0.185 | 6.62 | 6.69 | 7.47 | 112 000 | 60 500 | 6440 | VA—168 h at 200°C |
| 16EB12S | 0.194 | 4.29 | 4.35 | 4.70 | 123 000 | 60 500 | 6750 | VA—48 h at 239°C |
| 16EB7 | 0.207 | 2.45 | 2.45 | 2.70 | 76 200 | 40 400 | 4550 | VA—48 h at 239°C |
| 16DCD | 0.209 | 52.4 | 52.4 | 52.4 | 18 100 | 13 200 | 3690 | As grown |
| 24AC15 | 0.216 | 2.43 | 2.44 | 2.71 | 97 900 | 42 000 | 4250 | VA—142 h at 232°C |
| 18IB-1 | 0.220 | 14.7 | 14.7 | 14.7 | 50 300 | 30 000 | 4320 | As grown |
| 18IB-2 | 0.220 | 2.68 | 2.73 | 3.12 | 77 500 | 38 400 | 3760 | VA—24 h at 200°C |
| 18IB-3 | 0.220 | 74.9 | 74.9 | 74.9 | 17 100 | 13 100 | 3620 | Hg—45 h at 225°C |
| 16EB4-2 | 0.225 | ··· | 2.98 | 3.30 | ··· | 31 600 | 3750 | VA—48 h at 239°C |
| 16EA6 | 0.228 | 3.75 | 3.75 | 4.18 | 50 400 | 28 000 | 4070 | VA—48 h at 239°C |
| 23DB9 | 0.236 | 19.3 | 19.6 | 20.9 | 35 100 | 21 600 | 3610 | As grown |
| 23DA17 | 0.245 | 24.8 | 25.3 | 26.6 | 30 300 | 19 200 | 3550 | As grown |
| 18LF | 0.248 | 2.30 | 2.30 | 2.30 | 65 800 | 31 900 | 3500 | VA—64 h at 240°C |
| 24AB14 | 0.251 | 11.2 | 12.2 | 13.8 | 39 100 | 19 800 | 2590 | VA—93 h at 240°C |
| 18LG | 0.253 | 3.04 | 3.20 | 3.91 | 46 600 | 25 700 | 3290 | VA—93 h at 240°C |
| 26BB-1 | 0.268 | 11.9 | 11.9 | 11.9 | 23 200 | 15 600 | 3200 | As grown |
| 26BB-2 | 0.268 | 5.89 | 5.89 | 5.89 | 36 600 | 18 500 | 3250 | VA—24 h at 200°C |
| 26BB-3 | 0.268 | 28.4 | 28.4 | 28.4 | 15 200 | 10 900 | 2940 | Hg—45 h at 225°C |
| 4OEF3A | 0.272 | 23.0 | 23.0 | 23.0 | 23 600 | 15 600 | 3210 | VA—48 h at 220°C |
| 24AC13 | 0.297 | 1.27 | 1.27 | 1.27 | 27 300 | 17 900 | 2820 | As grown |
| 28AT253 | 0.300 | 9.57 | 9.57 | 9.57 | 19 600 | 12 700 | 2640 | Se—70 h at 250°C |
| 40EF3A | 0.332 | 13.6 | 13.6 | 13.6 | 12 000 | 8410 | 2050 | VA—48 h at 220°C |
| 40EC2 | 0.347 | ··· | 15.8 | 15.2 | ··· | 10 700 | 2320 | VA—64 h at 267°C |
| 24AA1-1 | 0.352 | 1.02 | 1.02 | 1.02 | 15 700 | 12 700 | 2400 | VA—67 h at 260°C |
| 24AA1-2 | 0.352 | 0.843 | 0.843 | 0.843 | 12 700 | 12 200 | 2390 | VA—67 h at 260°C +93 h at 240°C |
| 28AT10 | 0.354 | 8.62 | 8.62 | 8.62 | 11 600 | 8 350 | 2160 | As grown |
| 23DA3 | 0.361 | 23.5 | 23.3 | 23.8 | 7 230 | 5 740 | 1940 | As grown |
| 24AA3-5 | 0.366 | 31.0 | 31.0 | 31.0 | 5 050 | 4 210 | 1780 | As grown |
| 28ATE8 | 0.407 | 4.77 | 4.77 | 4.77 | 7 510 | 6 350 | 1800 | VA—25 h at 313°C |
| 28ATE7 | 0.412 | 5.19 | 5.19 | 5.19 | 8 470 | 6 880 | 1890 | VA—25 h at 313°C |
| 28ATE5A-5 | 0.430 | 0.676 | 0.720 | 0.960 | 1 050 | 2 380 | 989 | VA—184 h at 313°C +52 h at 302°C +168 h at RT in air |
| 28ATE5A-1 | 0.430 | ··· | ··· | 5.73 | ··· | ··· | 1640 | VA—141 h at 313°C |
| 28ATE5B-1 | 0.430 | ··· | ··· | 7.62 | ··· | ··· | 1420 | VA—141 h at 313°C |
| 28ATE5B-4 | 0.430 | (1.61) | 0.231 | 0.117 | ··· | ··· | 709 | VA—184 h at 313°C +52 h at 302°C +24 h at RT in air |
| 28ATE4 | 0.447 | 3.74 | 3.74 | 3.74 | 4 700 | 4 700 | 1470 | VA—194 h at 313°C +52 h at 303°C +200 h at 214°C |
| 28ATE0 | 0.499 | 2.28 | 2.24 | 2.46 | 2 350 | 3 610 | 1230 | VA—68 h at 313°C +52 h at 303°C +200 h at 214°C |
| 40EB2 | 0.547 | 5.16 | 5.16 | 5.16 | 2 590 | 3 100 | 1120 | VA—64 h at 267°C |
| 33AT1 | 0.600 | 3.29 | 3.44 | 4.58 | 703 | 2 775 | 1035 | As grown |
| 40EA2 | 0.684 | 2.33 | 2.33 | 2.76 | ··· | 2 130 | 763 | VA—64 h at 267°C |

[a] VA—vacuum anneal Hg—Hg anneal.

from mass density measurements. Complete temperature dependences from 4.2 to 300 K of the electron mobility were determined for most of the samples listed in Table I, and such data are shown and discussed later in this paper.

Some of the small $x$ samples have a temperature-dependent conduction-electron concentration. The temperature dependences observed are in substantial agreement with those calculated assuming the Kane energy-band model with the energy-band parameters determined in Ref. 12.

Some samples with higher $x$ values were unstable in air after they were annealed in a dynamic vacuum. The conduction-electron concentration decreased with time while simultaneously the electron mobility decreased. One sample, 28ATE5B-4 in Table I, had an electron concentration at 300 K of $1.17 \times 10^{15}$ per $cm^3$ after exposure to air and was $p$-type at 4.2 K. Another sample, 28ATE5A, also had a significantly lower electron concentration after exposure to air but remained $n$-type at 4.2 K. Some of these had Hall coefficients which were nonmonotonic functions of temperature. This electrical behavior strongly suggests an increasing level of compensation resulting from exposure to air, with the acceptor-type defects inhomogeneously distributed in the sample. We speculate that oxygen is introduced as an acceptor, as has been found[20] to occur in CdSe. Because of the suspected inhomogeneity in the acceptor concentrations, the low-temperature mobilities of these air exposed samples are not included in the analysis of the electron scattering mechanisms.

## III. ANALYSIS OF THE MOBILITY DATA

In this section, the observed mobilities are analyzed in terms of a microscopic theory of electrical conduction to define the fundamental scattering mechanisms limiting the electron mobility and to obtain information about the defect structure of the alloy system. A virtual crystal model is assumed whose "average" periodic potential yields a definable band structure, which is described by $\vec{k}\cdot\vec{p}$ theory with the aid of the experimental energy gaps presented in Ref. 12. In this model, the only remaining effect of the random short-range potential associated with the compositional disorder in the alloy is the scattering of the electrons among eigenstates of the virtual crystal Hamiltonian.

The use of adjustable parameters has been avoided wherever possible. Aside from the inevitable uncertainties about the kinds and densities of defects in a given sample, the most important unknown parameter is one associated with the random short-range alloy potential. This is defined with the aid of an *a priori* estimate and by requiring internal consistency over the ranges of compositions and temperatures investigated.

### A. Band structure

The Kane three-band model[16] is used to desribe the band structure in the energy range of interest, the highest-lying valence bands and lowest-lying conduction band. This approximation calculates energies and wave functions via the $\vec{k}\cdot\vec{p}$ interaction of $\Gamma_6$, $\Gamma_7$, and $\Gamma_8$. The results are specialized to the case of the normal band ordering ($E_{\Gamma_6} > E_{\Gamma_8}$), the transport properties of the inverted structure having been treated in Refs. 3, 4, and 17. The higher-band correction[4] to the conduction-band energy is ignored because for HgSe the matrix element involved in this correction for the $s$-like part of the wave function is (experimentally) found to be vanishingly small.[21] Thus, the correction should be negligible at the bottom of the conduction band for the normally ordered band structure of the alloy. The free-electron correction is also ignored. The secular equation describing the conduction band, light-hole band, and split-off valence band is given by

$$E^3 + (\Delta - E_g)E^2 - (E_g\Delta + P^2k^2)E - \tfrac{2}{3}\Delta P^2k^2 = 0, \quad (1)$$

where $\Delta$ is the $\Gamma_{15}$ spin-orbit splitting, $E_g$ is the $\Gamma_6$-$\Gamma_8$ band gap and $P$ is the momentum matrix element between the $\Gamma_{15}$ valence-band and the $\Gamma_1$ conduction-band wave functions defined by Kane.[16] The energy is referred to the top of the valence bands. The heavy-hole band is represented as a simple parabolic band of effective-mass ratio $\mu_v$. The conduction-band density of states is given by

$$\rho_c = [(2E_g)^{1/2}(\mu' m_0)^{3/2}/8\pi^3\hbar^3]\lambda_c(\xi), \quad (2)$$

where

$$\mu' = 3\hbar^2 E_g/4m_0P^2, \quad (3)$$

$$\lambda_c(\xi) = \frac{3[2\delta^2\xi^3 + \delta(3-\delta)\xi^2 + \frac{4}{3}(1-\delta)\xi - \frac{2}{3}][\xi(\xi-1)(\delta\xi+1)]^{1/2}}{2(\frac{3}{2}\delta\xi+1)^{5/2}}, \quad (4)$$

$$\xi = E/E_g, \quad (5)$$

and

$$\delta = E_g/\Delta. \quad (6)$$

Similarly, the crystal momentum as a function of energy is given by

$$k = (2\mu' m_0 E_g/\hbar^2)^{1/2} s(\xi)\,, \tag{7}$$

where

$$s(\xi) = [\xi(\xi-1)(\delta\xi+1)/(\tfrac{3}{2}\delta\xi+1)]^{1/2}\,. \tag{8}$$

The conduction-band wave functions are given by

$$|\vec{k}, c, \pm\rangle = e^{i\vec{k}\cdot\vec{r}}[a\,|iS\alpha_{\mp}\rangle \pm b\,|(X \mp iY)\alpha_{\pm}\rangle + c\,|Z\alpha_{\mp}\rangle]\,, \tag{9}$$

where $X$, $Y$, and $Z$ are the basis set of $\Gamma_{15}$ referred to a coordinate system with the $z$ axis along $\vec{k}$, $S$ is the $\Gamma_1$ wave function, $\alpha_{\pm}$ are Pauli spin functions for spin parallel (+) and anti-parallel (–) to $\vec{k}$, and $a$, $b$, and $c$ are functions defined by

$$a = [\xi(\delta\xi+1)(\delta\xi+\tfrac{2}{3})]^{1/2}/N\,, \tag{10}$$

$$b = \sqrt{2}\,(\xi-1)^{1/2}/3N\,, \tag{11}$$

and

$$c = (\xi-1)^{1/2}(\delta\xi+\tfrac{2}{3})/N\,, \tag{12}$$

where

$$N = [\xi(\delta\xi+1)(\delta\xi+\tfrac{2}{3}) + \tfrac{2}{9}(\xi-1) + (\xi-1)(\delta\xi+\tfrac{2}{3})^2]^{1/2}\,. \tag{13}$$

The numerical values of the band parameters used in the calculations are as follows. The temperature and composition dependences of the band gap determined in Ref. 12 are well approximated (in electron volts) by the expression

$$E_g(x,T) = 0.505x^2 + 1.54x - 0.22 + (9.684 - 17.72x)\times 10^{-4}T\,. \tag{14}$$

For the spin-orbit splitting $\Delta$ we use a linear interpolation between the HgSe value[21] (0.45) and the CdSe value[5] (0.43). The momentum matrix-element $P$ is approximately the same in both HgSe (Ref. 21) and CdSe (Ref. 22), and we use the value $7.2\times10^{-8}$ eV cm throughout. The HgSe value[4] of $0.78m_0$ is used for the heavy-hole mass $\mu_v$.

The Fermi energy $E_F$, electron concentration $n_e$, heavy-hole concentration $n_{hh}$, and light-hole concentration $n_{lh}$, are calculated from the numerical solution of the charge neutrality equation

$$n_e - n_{lh} - n_{hh} = N_D - N_A\,, \tag{15}$$

where

$$n_e = \frac{1}{2\pi^2}\left(\frac{2\mu' m_0 k_B T}{\hbar^2}\right)^{3/2}\frac{1}{\beta^{1/2}}\int_{\beta^{-1}}^{\infty} dy\, f_0(y,z)\lambda_c(\beta y)\,, \tag{16}$$

$$n_{lh} = \frac{1}{2\pi^2}\left(\frac{2\mu' m_0 k_B T}{\hbar^2}\right)^{3/2}\frac{1}{\beta^{1/2}}\int_{0}^{\infty} dy f_0(y,-z)\lambda_v(\beta y)\,, \tag{17}$$

$$n_{hh} = \frac{1}{2\pi^2}\left(\frac{2\mu_v m_0 k_B T}{\hbar^2}\right)^{3/2} F_{1/2}(-z)\,, \tag{18}$$

$$\lambda_v(\xi) = 3[2\delta^2\xi^3 - \delta(3-\delta)\xi^2 + \tfrac{4}{3}(1-\delta)\xi + \tfrac{2}{3}] \times[\xi(\xi+1)(\delta\xi-1)]^{1/2}/2(\tfrac{3}{2}\delta\xi-1)^{5/2}\,, \tag{19}$$

$$z = E_F/k_B T\,, \tag{20}$$

$$\beta = k_B T/E_g\,, \tag{21}$$

$$f_0(y,z) = (e^{y-z}+1)^{-1}\,, \tag{22}$$

and $F_{1/2}(z)$ is the Fermi function of order $\frac{1}{2}$. Because no carrier freeze out is observed, the donor and acceptor concentrations, $N_D$ and $N_A$, are assumed to be independent of temperature.

### B. Scattering mechanisms and solution of the Boltzmann equation

The six scattering mechanisms which should be of importance in this alloy system are longitudinal-optical- (LO) phonon scattering, acoustical-phonon scattering, electron-hole scattering, scattering from electrically charged and neutral defects, and compositional disorder scattering. The nonpolar optical-phonon coupling discussed by Ehrenreich[23] is unimportant for this study because it vanishes at the bottom of the $\Gamma_6$ band. In this section, we formulate the Boltzmann equation for the electron distribution function and outline the calculation of the mobility.

The field term of the Boltzmann equation for a system driven by a static electric field $\vec{\mathcal{E}}$ is given by

$$\left(\frac{\partial f(\vec{k})}{\partial t}\right)_F = \frac{\mathcal{E}e}{\hbar} f_0' \frac{dE}{dk}\cos\theta\,, \tag{23}$$

where $\theta$ is the angle between $\vec{k}$ and $\vec{\mathcal{E}}$, $f(\vec{k})$ is the perturbed distribution function, and $f_0' = df_0/dE$. We assume that the form of the perturbed distribution function is given by

$$f(\vec{k}) = f_0 - kc'(E)f_0'\cos\theta\,, \tag{24}$$

where $c'(E)$ is a function only of the energy and is determined by the solution of the Boltzmann equation.

#### *1. Longitudinal-optical-phonon scattering*

In Ref. 13 the infrared spectrum of the alloy system in the region of the Restrahl band was found to consist of an extremely broadened, intense oscillator at about the HgSe transverse-optical (TO) phonon frequency which shifted strongly with alloy composition, and a weak, somewhat narrower oscillator at about the CdSe TO-phonon frequency. The data were analyzed in terms of a dielectric function of the form

$$\epsilon(\omega)=\epsilon_\infty+\sum_{i=1}^{2}\frac{F_i}{\omega_{Ti}^2-\omega^2+i\omega\Gamma_i}+\epsilon_{pl}, \tag{25}$$

where

$$F_i=\frac{4\pi N_i e_{Ti}^{*2}}{\bar{M}_i}. \tag{26}$$

Here $\omega_{Ti}$ is the TO-phonon frequency of the $i$th oscillator, $N_i$ is the number of unit cells of the $i$th type per unit volume, $e_{Ti}^*$ is the total transverse effective charge of the $i$th type of unit cell, $\bar{M}_i$ is the reduced mass of the $i$th unit cell, $\epsilon_\infty$ is the interband electronic dielectric function (high-frequency dielectric constant), $\Gamma_i$ is a broadening parameter, and $\epsilon_{pl}$ is the free-carrier plasma dielectric function. The composition dependence of the oscillator frequencies (in $cm^{-1}$) determined in Ref. 13 can be accurately represented by the empirical expressions

$$\omega_{T1}=55.54x^2-3.39x+134.43 \tag{27}$$

and

$$\omega_{T2}=33.59x^2-39.45x+189.76. \tag{28}$$

The experimentally determined oscillator strengths $S_i=F_i/\omega_{Ti}^2$ as functions of alloy composition are shown in Figs. 2 and 3. The $F_i$ are not proportional to $N_i$, which implies that the effective charges change with alloy composition. The curves in Figs. 2 and 3 are the fits to the data, which are used in the following calculations. In Fig. 4 are shown the experimentally determined values of the high-frequency dielectric constant. The two curves represent roughly a high fit (1) and a low fit (2) to the data. For well separated and unbroadened oscillators, there would exist two coupled longitudinal modes at frequencies

$$\omega_{L\pm}=\left(\frac{1}{2\epsilon_\infty}\left(\epsilon_\infty(\omega_{T1}^2+\omega_{T2}^2)+S_1\omega_{T1}^2+S_2\omega_{T2}^2\right.\right.$$
$$\left.\pm\{[\epsilon_\infty(\omega_{T1}^2-\omega_{T2}^2)+S_1\omega_{T1}^2-S_2\omega_{T2}^2]^2$$
$$\left.\left.+4\omega_{T1}^2\omega_{T2}^2S_1S_2\}^{1/2}\right)\right)^{1/2}. \tag{29}$$

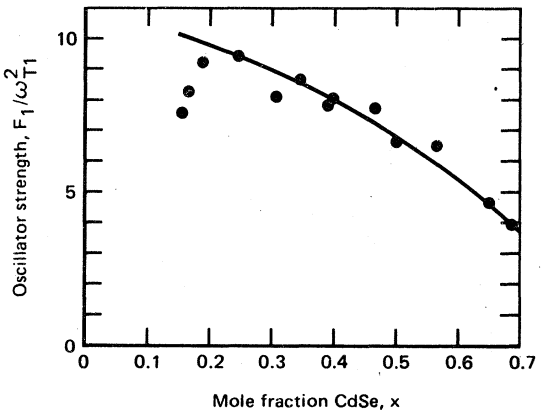


FIG. 2. Oscillator strength of the HgSe-like TO mode in the $Hg_{1-x}Cd_xSe$ alloy system as a function of alloy composition. $F_1$ is defined by Eq. (26) and experimental values of $\omega_{T1}$ are given by Eq. (27). The data are from Ref. 13, and the curve represents the fitted values used in the calculations of this paper.

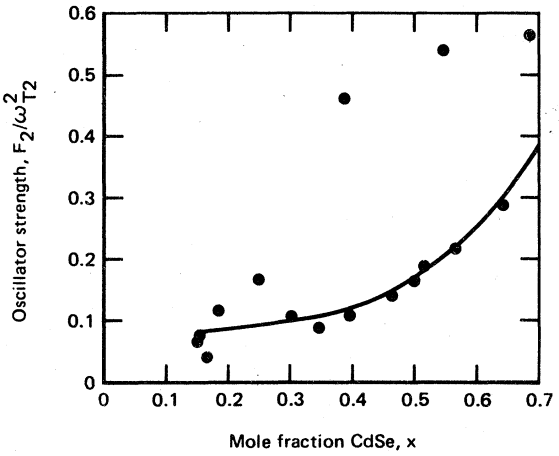


FIG. 3. Oscillator strength of the CdSe-like TO mode in the $Hg_{1-x}Cd_xSe$ alloy system as a function of alloy composition. $F_2$ is defined by Eq. (26) and experimental values of $\omega_{T2}$ are given by Eq. (28). The data are from Ref. 13, and the curve represents the fitted values used in the calculations of this paper.

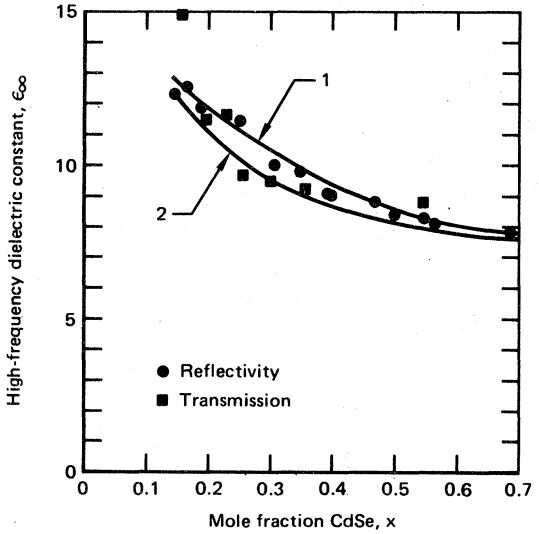


FIG. 4. High-frequency dielectric constant $\epsilon_\infty$ of the $Hg_{1-x}Cd_xSe$ alloy system as a function of alloy composition. The data are from Ref. 13, and the curves represent high (1) and low (2) fits to the data.

However, because of the extreme broadening and small separation of these modes, we regard them as a single mode of frequency

$$\omega_L = \tfrac{1}{2}(\omega_{L+} + \omega_{L-}). \tag{30}$$

The dielectric function that screens the electron-LO-phonon interaction is given by

$$\epsilon(\omega_L, q) = \epsilon_\infty + \frac{(k_{FT}^e)^2 + (k_{FT}^{lh})^2}{q^2}, \tag{31}$$

where the electron and light-hole Fermi-Thomas momenta are given by

$$(k_{FT}^e)^2 = \frac{2e^2}{\pi}\left(\frac{2\mu' m_0}{\hbar^2}\right)^{3/2}\left(\frac{k_B T}{\beta}\right)^{1/2} \times \int_{\beta^{-1}}^{\infty} dy \lambda_c(y) \frac{e^{y-\varepsilon}}{(e^{y-\varepsilon}+1)^2}, \tag{32}$$

$$(k_{FT}^{lh})^2 = \frac{2e^2}{\pi}\left(\frac{2\mu' m_0}{\hbar^2}\right)^{3/2}\left(\frac{k_B T}{\beta}\right)^{1/2} \times \int_{0}^{\infty} dy \lambda_v(y) \frac{e^{y+\varepsilon}}{(e^{y+\varepsilon}+1)^2}, \tag{33}$$

respectively. Equation (31) ignores the modification to the Fermi-Thomas screening discussed by Broerman, Liu, and Pathak[24] because for all samples considered here, the electron gas is nondegenerate at temperatures for which the LO-phonon scattering is important, and under this condition, the expression of Eq. (31) is exact within the random-phase approximation. The small antiscreening by the heavy holes, discussed by Lehoczky[4] *et al.*, is neglected.

Following Ehrenreich,[23] the collision term of the Boltzmann equation for the $i$th type LO-phonon interaction is given by

$$\left(\frac{\partial f}{\partial t}\right)_{LO(i)} = -\frac{4\pi(e_c^* e)^2 \mu' m_0}{\hbar^2 \bar{M} \omega_L \lambda_c s E_g} N_i k_B T \mathcal{L}_{LO}(c') f_0' \cos\theta, \tag{34}$$

where

$$\mathcal{L}_{LO}(c') = \beta^{-1}[(f_+/f_0)(n_p+1)(c'_+ R_+ - c' S_+) + (f_-/f_0) n_p (c'_- R_- - c' S_-)]. \tag{35}$$

Here the subscripts (±) refer to the evaluation of the function at $y \pm \theta$, where $y = E/k_B T$ and $\theta = \hbar\omega_L/k_B T$. The function $n_p$ is the phonon occupation number,

$$n_p = (e^\theta - 1)^{-1}. \tag{36}$$

The functions $R_\pm$ and $S_\pm$ are defined in the Appendix. The effective charge $e_c^*$, which appears in Eq. (34), is the Callen effective charge, and it is related to the Szigetti effective charge $e_s^*$ and the total transverse charge $e_T^*$ by

$$e_c^* = [(\epsilon_\infty + 2)/3\epsilon_\infty] e_s^* = e_T^*/\epsilon_\infty. \tag{37}$$

In terms of the experimentally determined $F_i$, the Boltzmann equation has the form,

$$\left(\frac{\partial f}{\partial t}\right)_{LO} = -\frac{e^2 \mu' m_0 k_B T F}{\hbar^2 \omega_L \lambda_c s E_g \epsilon_\infty^2} \mathcal{L}_{LO}(c') f_0' \cos\theta, \tag{38}$$

where $F = F_1 + F_2$. Thus, within this approximation, the LO-phonon contribution to the scattering depends only on experimentally determined quantities.

### 2. *Acoustical-phonon scattering*

The acoustical-phonon interaction is described by the treatment of Zawadzki and Szymanska,[25] which includes the interaction with both longitudinal and transverse phonons. The interaction is characterized by three deformation potentials: $E_0$ for the longitudinal mode and $E_1$ and $E_2$ for the transverse modes. The acoustical-phonon contribution to the Boltzmann equation is given by

$$\left(\frac{\partial f(\vec{k})}{\partial t}\right)_{ac} = \frac{2k_B T E_0^2}{\pi\hbar^5 d v_L^2} (\mu' m_0)^2 E_g \lambda_c s \times \left[F_L + \left(\frac{v_L}{v_T}\right)^2 F_T\right] f_0' \cos\theta\, c'(E), \tag{39}$$

where $d$ is the mass density of the material, and $v_L$ and $v_T$ are the longitudinal and transverse velocities of sound, respectively. The functions $F_L$ and $F_T$ are defined in Ref. 4. We use the following expressions for the parameters[6,26,27]:

$$d = \frac{4[112.4x + (1-x)200.59 + 78.96]}{[(6.0855 - 0.004x) \times 10^{-8}]^3} \times 1.6605655 \times 10^{-24} \text{ cm}^3, \tag{40}$$

$$v_L = (2.9 + 0.9x) \times 10^5 \text{ cm/sec}, \tag{41}$$

$$v_T = (1.7 - 0.2x) \times 10^5 \text{ cm/sec}. \tag{42}$$

For the deformation potentials,[28,29] we use $E_0 = 11$ eV, $E_1 = 5$ eV, and $E_2 = 1.75$ eV. The value for $E_0$ is an estimate based on the values for[29] CdSe and[28] HgTe, which is similar in most respects to HgSe. The values for $E_1$ and $E_2$ correspond to the hydrogenic approximation discussed by Zawadzki and Szymanska.[25] For the normally ordered band structure of the alloy, the acoustical-phonon contribution to the scattering is almost entirely determined by $E_0$, and for the $E_0$ value used, acoustical scattering is a negligible contribution to the total scattering. An error of 20% in $E_0$ changes the total calculated mobility by about 1%.

### 3. Ionized impurity and electron-hole scattering

The electron-ionized-defect interaction is screened by the dielectric function,

$$\epsilon(q)=\epsilon_0+\frac{1}{q^2}\left[(k_{\mathrm{FT}}^{e})^2+(k_{\mathrm{FT}}^{\mathrm{lh}})^2+(k_{\mathrm{FT}}^{\mathrm{hh}})^2\right], \tag{43}$$

where $k_{\mathrm{FT}}^{\mathrm{hh}}$ is the heavy-hole Fermi-Thomas momentum, given by

$$(k_{\mathrm{FT}}^{\mathrm{hh}})^2=\frac{e^2}{\pi}\left(\frac{2\mu_v m_0}{\hbar^2}\right)^{3/2}(k_B T)^{1/2}F_{-1/2}(-z), \tag{44}$$

$\epsilon_0$ is the low-frequency dielectric constant, and $F_{-1/2}$ is the Fermi function of order $-\frac{1}{2}$. The dependence of low-frequency dielectric constant on alloy composition was measured in Ref. 13, and we approximate it by the empirical expression,

$$\epsilon_0=23.8-16.7x. \tag{45}$$

The contribution to the Boltzmann equation from ionized-impurity scattering is

$$\left(\frac{\partial f(\vec{k})}{\partial t}\right)_{\mathrm{ii}}=\frac{\pi(N_D Z_D^2+N_A Z_A^2)e^4\lambda_c}{\hbar\epsilon_0^2 E_g s^3}\Phi_{\mathrm{ii}} f_0' \cos\theta\, c'(E), \tag{46}$$

where $N_D$ and $N_A$ are the donor and acceptor concentrations, respectively, and $Z_D$ and $Z_A$ are their charges in electron-charge units. The function $\Phi_{\mathrm{ii}}$ is given in Ref. 4 with the replacement

$$g_0^2=\frac{\hbar^2[(k_{\mathrm{FT}}^{e})^2+(k_{\mathrm{FT}}^{\mathrm{lh}})^2+(k_{\mathrm{FT}}^{\mathrm{hh}})^2]}{2\mu' m_0 E_g\epsilon_0}. \tag{47}$$

It is assumed that the electron heavy-hole interaction is screened by the high-frequency dielectric function of Eq. (31), and that the effects of electron light-hole scattering are negligible. The contribution to the Boltzmann equation from electron-hole scattering is then given by Eq. (46) with $\epsilon_0$ replaced by $\epsilon_\infty$, $(Z_D^2 N_D+Z_A^2 N_A)$ replaced by $n_{\mathrm{hh}}$, and $g_0$ replaced by $g_\infty$.

### 4. Compositional-disorder and neutral-defect scattering

Although it is implicitly assumed that the band structure of the alloy is given by a virtual crystal or average periodic potential and is described by the Kane theory, there remains a random short-range potential resulting from compositional disorder which will produce electron scattering. This scattering is treated using a modification of a theory attributed to Brooks (quoted in Ref. 30). The theory treats the compositional disorder as a random distribution of square-well scattering centers, which have unit-cell dimensions and depths approximately equal to the difference in band gaps of the end-point compounds. In our formalism, the contribution to the Boltzmann equation from this process is given by

$$\left(\frac{\partial f(\vec{k})}{\partial t}\right)_{\mathrm{dis}}=\frac{E_g}{\pi\hbar^5}(\mu' m_0)^2 s\lambda_c\frac{x(1-x)E_{\mathrm{dis}}^2}{N_a}\Phi_{\mathrm{dis}} c' f_0' \cos\theta, \tag{48}$$

where $N_a$ is the number of unit cells per unit volume, $E_{\mathrm{dis}}$ is the disorder potential, approximately equal to the difference in end-point band gaps (in this case, the difference between the $E_{\Gamma_6}-E_{\Gamma_8}$ values for HgSe and CdSe, or 2 eV), and $\Phi_{\mathrm{dis}}$ is a wave-function-overlap integral given by

$$\Phi_{\mathrm{dis}}=2a^4+b^4+\tfrac{2}{3}c^4-\tfrac{4}{3}\sqrt{2}\,b^3c+4b^2c^2-\tfrac{4}{3}a^2(b^2+c^2). \tag{49}$$

If there is also present a dilute distribution of short-range neutral-scattering centers, describable by square-well potentials of dimensions small with respect to $1/q_{\max}$ (the maximum momentum transfer), then the contribution of these centers to the scattering is also given by Eq. (48) with $x(1-x)E_{\mathrm{dis}}^2/N_a$ replaced by $N_n v_n^2 E_n^2$, where $N_n$ is the density of square-well scatterers, $v_n$ is the volume of the potential well, and $E_n$ is the strength.

### 5. Solution of the Boltzmann equation

The complete scattering contribution to the Boltzmann equation from all the scattering mechanisms is

$$\left(\frac{\partial f(\vec{k})}{\partial t}\right)_{\mathrm{scat}}=-\frac{e^2\mu' m_0 k_B TF}{\hbar^2\omega_L\lambda_c s E_g\epsilon_\infty^2}\mathcal{L}(c')f_0'\cos\theta, \tag{50}$$

where

$$\mathcal{L}(c')=\mathcal{L}_{\mathrm{LO}}(c')-\Big\{a_{\mathrm{ac}}\lambda_c^2 s^2\left[F_L+\left(\frac{v_L}{v_T}\right)^2 F_T\right]+a_{\mathrm{ii}}\frac{\lambda_c^2}{s^2}\Phi_{\mathrm{ii}}+a_{e\text{-}h}\frac{\lambda_c^2}{s^2}\Phi_{\mathrm{eh}}+(a_{\mathrm{dis}}+a_n)\lambda_c^2 s^2\Phi_{\mathrm{dis}}\Big\}c'(E), \tag{51}$$

$$a_{\mathrm{ac}}=2E_0^2\mu' m_0 E_g\omega_L\epsilon_\infty^2/\pi\hbar^3 d v_L^2 e^2 F, \tag{52}$$

$$a_{\mathrm{ii}}=(\pi\hbar e^2\omega_L\epsilon_\infty^2/\mu' m_0 k_B TF\epsilon_0^2)(Z_D^2 N_D+Z_A^2 N_A), \tag{53}$$

$$a_{e\text{-}h}=(\pi\hbar e^2\omega_L/\mu' m_0 k_B TF)n_{\mathrm{hh}}, \tag{54}$$

$$a_{\mathrm{dis}}=(E_g^2\mu' m_0\omega_L\epsilon_\infty^2 E_{\mathrm{dis}}^2/\pi\hbar^3 e^2 k_B TFN_a)x(1-x), \tag{55}$$

and

$$a_n=(E_g^2\mu' m_0\omega_L\epsilon_\infty^2/\pi\hbar^3 e^2 k_B TF)N_n v_n^2 E_n^2. \tag{56}$$

Under steady-state conditions, when $(\partial f/\partial t)_{\text{field}} + (\partial f/\partial t)_{\text{scat}} = 0$, the Boltzmann equation reduces to the linear finite-difference equation,

$$\mathcal{L}(c') = \frac{2^{1/2}\mathcal{E}\hbar^2\omega_L\epsilon_\infty^2}{e(\mu' m_o)^{3/2}F}(k_B T)^{1/2}\frac{s^2}{\beta^{3/2}}. \tag{57}$$

We calculate the conductivity from the Boltzmann equation by using the variational method of Kohler,[31] as generalized to nonparabolic band shapes by Ehrenreich.[23] The perturbation function $c'(E)$ is expanded in a complete set of trial functions

$$c'(E) = \sum_{n=0}^{\infty} c_n \phi_n(E), \tag{58}$$

and the $c_n$ are determined by the requirement that $c'(E)$ be a stationary point[31] of a certain conserved integral. The set,

$$\phi_n = (y - \beta^{-1})^n, \tag{59}$$

is used for the trial functions, and the expansion is carried to third order ($n = 2$).

The $c_n$ completely determine $f(\vec{k})$, from which the current density $j$ and conductivity $j/\mathcal{E}$ are calculated. The result for the conductivity is

$$\sigma = \frac{4\epsilon_\infty^2\omega_L(k_B T)^2}{3\pi^2\hbar^2 F}\left(\frac{L^{(0)2}}{F_{00}} + \frac{[(\mathcal{L},l)_1]^2}{\mathcal{L}_2\mathcal{L}_1} + \frac{[(\mathcal{L},l)_2]^2}{\mathcal{L}_3\mathcal{L}_2} + \cdots\right). \tag{60}$$

where

$$\mathcal{L}_{n+1} = \begin{vmatrix} F_{00} & F_{01} & \cdots & F_{0n} \\ \vdots & \vdots & & \vdots \\ F_{n0} & F_{n1} & \cdots & F_{nn} \end{vmatrix}, \tag{61}$$

$$(\mathcal{L},l)_n = \begin{vmatrix} F_{00} & \cdots & F_{0,n-1} & L^{(0)} \\ \vdots & & \vdots & \vdots \\ F_{n-1,0} & \cdots & F_{n-1,n-1} & L^{(n-1)} \\ F_{n,0} & \cdots & F_{n,n-1} & L^{(n)} \end{vmatrix}, \tag{62}$$

$$F_{mn} = \int_{\beta^{-1}}^{\infty} \phi_m \mathcal{L}(\phi_n) f_0' \, dy, \tag{63}$$

and

$$L^{(m)} = \int_{\beta^{-1}}^{\infty} \phi_m f_0' \frac{s^3}{\beta^{3/2}} dy. \tag{64}$$

The drift mobility is within a few percent of the Hall mobility $\mu_H$ for these scattering mechanisms, and thus

$$\mu_H \approx \frac{\sigma}{n_e e}. \tag{65}$$

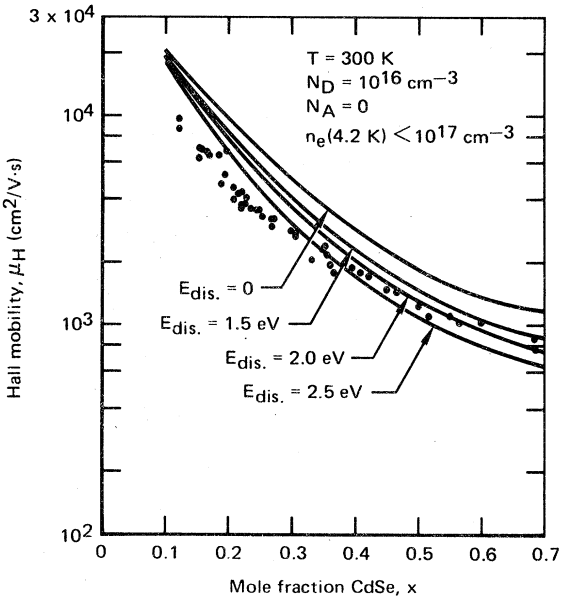


FIG. 5. 300-K Hall mobilities of $Hg_{1-x}Cd_xSe$ samples as a function of alloy composition. The theoretical curves are calculated with the high fit for $\epsilon_\infty$ (curve 1 of Fig. 4) for various values of the disorder potential $E_{\text{dis}}$ assuming $10^{16}\text{cm}^{-3}$ donors, no acceptors and no neutral defects.

### C. Comparison of theory and experiment

We first consider the room-temperature data, where intrinsic scattering processes (LO-phonon, acoustical-phonon, electron-hole, and compositional-disorder scattering) are expected to dominate the extrinsic processes (defect scattering). Aside from the experimental uncertainties in the lattice oscillator strengths and the dielectric constants, the only adjustable parameter is the disorder potential, $E_{\text{dis}}$. In Fig. 5 are shown the 300-K experimental mobilities as a function of composition along with the theoretical values calculated for various values of $E_{\text{dis}}$. We have used the high fit for $\epsilon_\infty$ (curve 1 of Fig. 4) in the calculation because it gives the best fit for $E_{\text{dis}} = 2$ eV. The theoretical mobilities at 300 K are nearly independent of electron concentration, and the calculations assume a donor density $N_D$ of $10^{16}$ cm$^{-3}$ and no acceptors or neutral defects. The mobility values calculated with $E_{\text{dis}} = 2$ eV are in good agreement with the data, the highest mobility samples in every composition range lying within 10%–15% of the theoretical curve.

This interpretation of the electron-transport properties encounters a serious problem when the low-temperature mobility in the mid-$x$ range is examined. In Fig. 6 are shown experimental and theoretical mobilities between 4.2 and 300 K for a

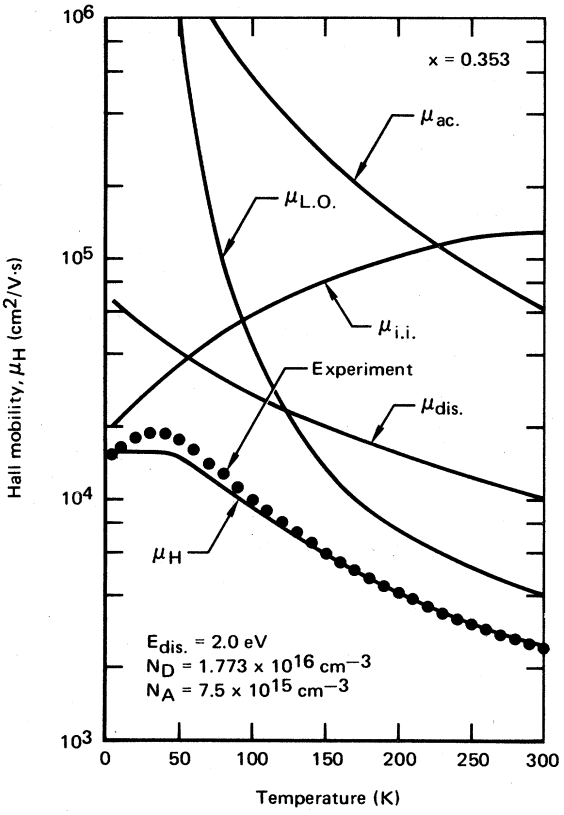


FIG. 6. Hall mobility as a function of temperature of sample 24AA1 with $x = 0.353$ and $n_e$ (4.2 K) = $1.02 \times 10^{16}$ $cm^{-3}$. The theoretical curve for $\mu_H$ was calculated with the high fit for $\epsilon_\infty$ (curve 1 of Fig. 4) and the value of 2.0 eV for the disorder potential $E_{dis}$. The sample was assumed to have no neutral defects and to be compensated to a level necessary to match the observed 4.2-K mobility. Also shown are the contributions to the mobility of the individual scattering mechanisms.

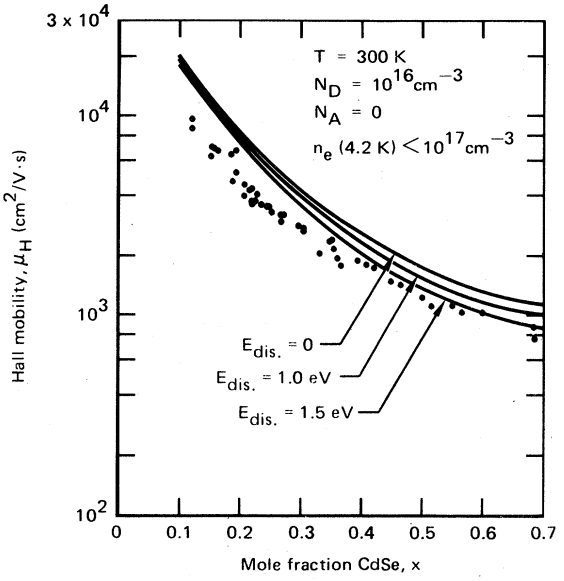


FIG. 7. 300-K Hall mobilities of $Hg_{1-x}Cd_xSe$ samples as a function of alloy composition. The theoretical curves are calculated with the low fit for $\epsilon_\infty$ (curve 2 of Fig. 4) for various values of the disorder potential $E_{dis}$ assuming $10^{16}$ $cm^{-3}$ donors, no acceptors and no neutral defects.

sample with $x = 0.353$. The mobility at 4.2 K for this sample is lower than that predicted for singly-ionized donors only, and thus acceptors were also included in the calculations subject to the condition $N_D - N_A = n_e$ (4.2 K). Also shown in Fig. 6 are the individual contributions of the various scattering mechanisms to the mobility (i.e., the mobility which would be found if only the indicated mechanism were present). The low-temperature peaking behavior of the observed mobility is characteristic of compensated samples in this range of effective mass, low-frequency dielectric constant, and carrier concentration. As the temperature increases and higher-energy states in the conduction band are populated, the higher momentum electrons are less efficiently scattered by the ionized-defects screened-Coulomb potential (which is reduced by increased free-electron screening), and the mobility increases until it is limited by the onset of other scattering mechanisms. This feature is not present in the calculated mobility. What is disturbing about this comparison is not so much the magnitude of the disagreement, which on the whole is rather small, but the fact that the shape of the calculated curve is qualitatively incorrect. The increase in the ionized-impurity-limited mobility is theoretically predicted, but the peak does not appear in the total mobility because the disorder scattering is sufficiently intense and increases rapidly enough with temperature to damp out the increase in total mobility.

The problem can be remedied by using a lower value for $E_{dis}$. In order to preserve the agreement at 300 K, we use a low fit for the high-frequency dielectric constant (curve 2 of Fig. 4). In Fig. 7 are shown experimental mobilities and calculated values (for three values of $E_{dis}$) as a function of composition at 300 K. The agreement for $E_{dis} = 1.5$ eV is quite good, the highest observed mobilities lying within about 12% of the calculated values. Similar agreement is obtained at 200 K, as is shown in Fig. 8. The results at 100 K are shown in Fig. 9, where the theoretical curves are for $N_D = 10^{16}$ $cm^{-3}$ and $10^{17}$ $cm^{-3}$, and all the data displayed is for samples with electron concentrations between these limits. Larger disagreement is to be expected at 100 K where extrinsic scattering mechanisms

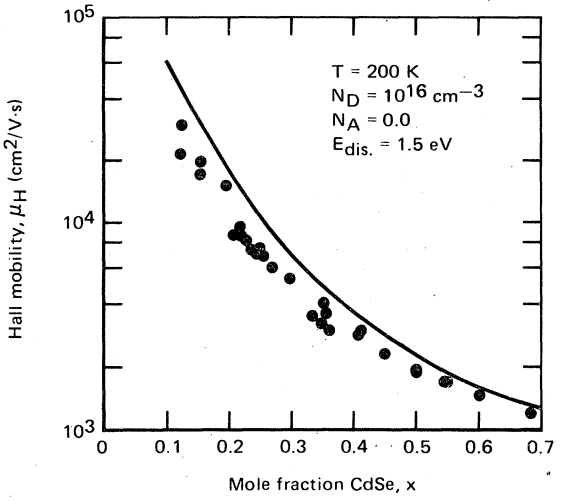


FIG. 8. 200-K Hall mobilities of $Hg_{1-x}Cd_xSe$ samples as a function of alloy composition. The experimental points are for samples with $n_e$ (4.2 K) between $10^{16}$ and $10^{17}$ cm$^{-3}$. The theoretical curve is calculated with the low fit for $\epsilon_\infty$, a value of 1.5 eV for the disorder potential $E_{dis}$, $10^{16}$ cm$^{-3}$ donors, no acceptors and no neutral defects.

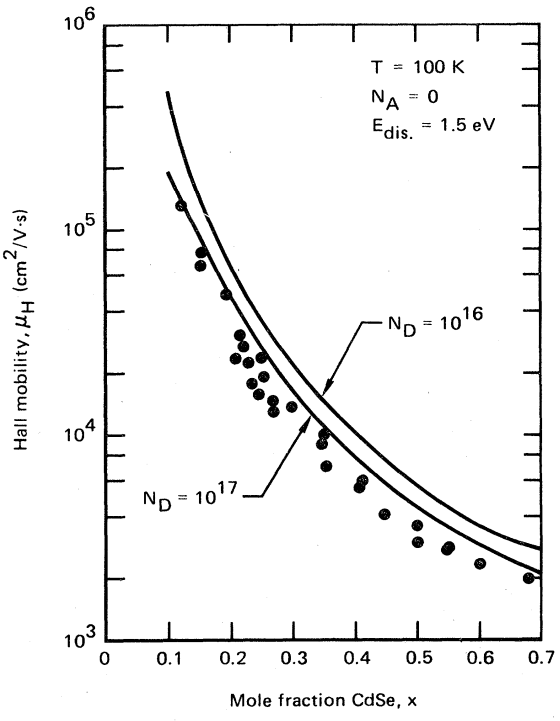


FIG. 9. 100-K Hall mobilities of $Hg_{1-x}Cd_xSe$ samples as a function of alloy composition. The experimental points are for samples with $10^{16}$ cm$^{-3} \leq n_e$ (4.2 K) $\leq 10^{17}$cm$^{-3}$. The theoretical curves are calculated with the low fit for $\epsilon_\infty$ (curve 2 of Fig. 4), a value of 1.5 eV for the disorder potential $E_{dis}$, $10^{16}$ cm$^{-3}$ and $10^{17}$ cm$^{-3}$ donors, no acceptors and no neutral defects.

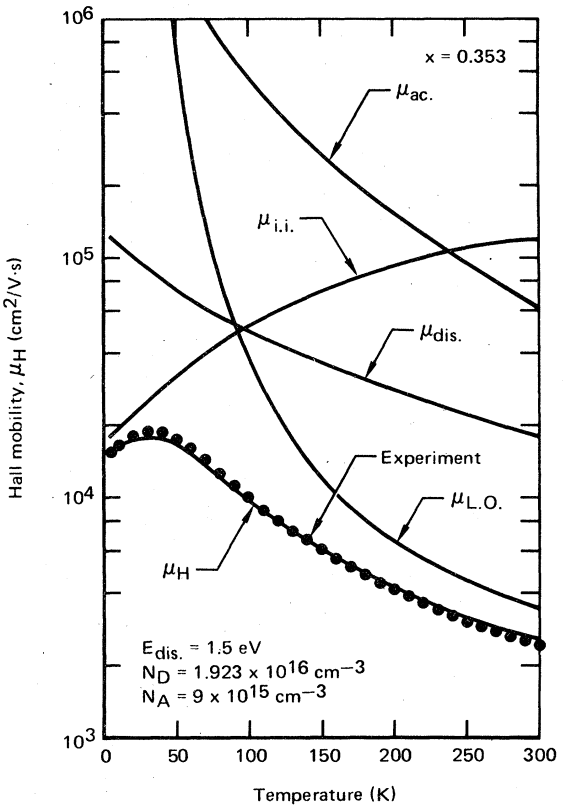


FIG. 10. Hall mobility as a function of temperature of sample 24AA1 with $x = 0.353$ and $n_e$ (4.2 K) $= 1.02 \times 10^{16}$ cm$^{-3}$. The theoretical curve for $\mu_H$ was calculated with the low fit for $\epsilon_\infty$ (curve 2 of Fig. 4) and the value of 1.5 eV for the disorder potential $E_{dis}$. The sample was assumed to nave no neutral defects and to be compensated to a level necessary to match the observed 4.2 K mobility. Also shown are the contributions to the mobility of the individual scattering mechanisms.

become important.

Returning now to the $x = 0.353$ sample, we show in Fig. 10 the results for $E_{dis} = 1.5$ eV and the low fit for $\epsilon_\infty$. The calculation now reproduces quite accurately the low-temperature peaking behavior seen in the data at about 40 K, and is in extraordinary agreement over the whole temperature range. In Fig. 11 are shown the results for a low-$x$ sample ($x = 0.194$). This sample was regarded as uncompensated and having no neutral defects. The data lie a nearly constant 12% below the theory over the entire temperature range. In Fig. 12 are shown results for a high-$x$ sample ($x = 0.547$). The theoretical curve is in excellent agreement at 300 K and shows qualitatively the peaking of the low-temperature mobility, with a maximum disagreement of about 15% (at 100 K). For this sample, better agreement would have been obtained with a

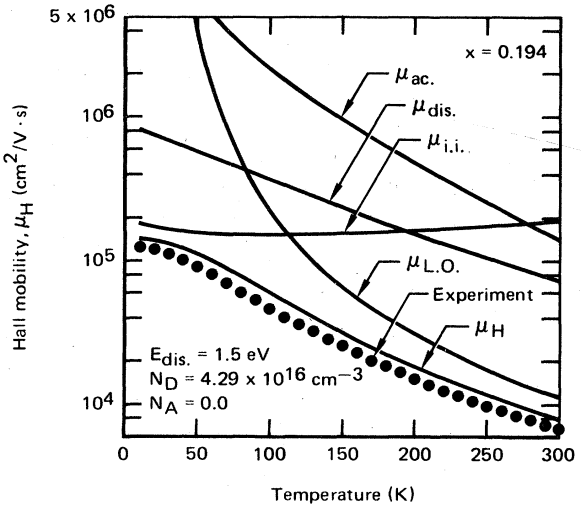


FIG. 11. Hall mobility as a function of temperature of sample 16EB12S with $x = 0.194$ and $n_e$ (4.2 K) = $4.29 \times 10^{16}$ $cm^{-3}$. The theoretical curve for $\mu_H$ was calculated with the low fit for $\epsilon_\infty$ (curve 2 of Fig. 4) and the value of 1.5 eV for the disorder potential $E_{dis}$. The sample was assumed to have no neutral defects and to be uncompensated. Also shown are the contributions to the mobility of the individual scattering mechanisms.

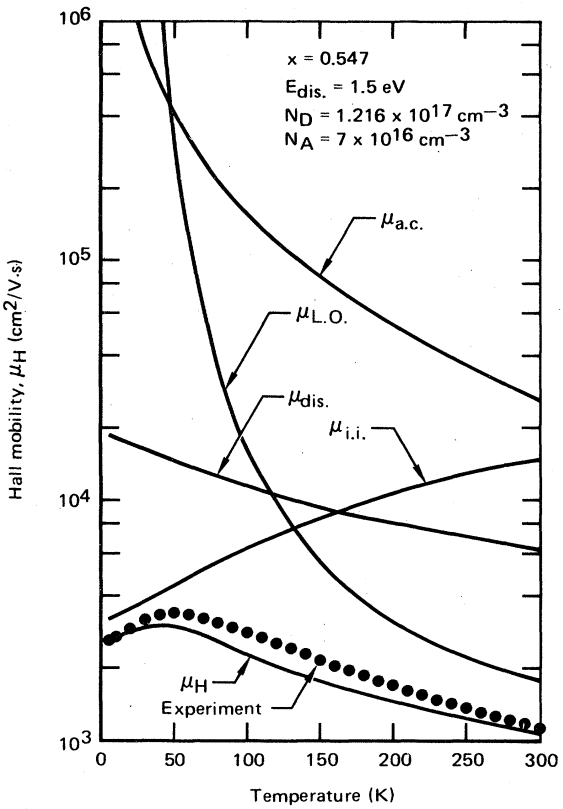


FIG. 12. Hall mobility as a function of temperature of sample 40EB2 with $x = 0.547$ and $n_e$ (4.2 K) = $5.16 \times 10^{16}$ $cm^{-3}$. The theoretical curve for $\mu_H$ was calculated with the low fit for $\epsilon_\infty$ (curve 2 of Fig. 4) and the value of 1.5 eV for the disorder potential $E_{dis}$. The sample was assumed to have no neutral defects and to be compensated to a level necessary to fit the observed 4.2-K mobility. Also shown are the contributions to the mobility of the individual scattering mechanisms.

slightly lower value of $E_{dis}$ (1.0–1.25 eV).

Thus, the mobilities of the "best" samples over the entire range of composition and temperature are accurately predicted by scattering primarily by LO-phonons, compositional disorder, and charged defects. Acoustical-phonon scattering is relatively unimportant in all cases. Higher-$x$ samples appear to have some compensating acceptors.

However, an inspection of Fig. 7 reveals a large number of samples below $x = 0.3$ whose mobilities cluster at about 40% below the theoretical curve, and these results cannot be explained by compensation. The densities of acceptors necessary to explain the 4.2-K mobilities of these samples produce relatively small contributions to the total scattering at 300 K because of the decrease in efficiency of scattering from charged centers with increasing temperature and the extremely strong electron–LO-phonon coupling. Thus, some other extrinsic scattering mechanism must be involved.

Sample 26BB ($x = 0.268$) is an example of the low mobility specimens. For this sample, we have a detailed annealing history. The as-grown 4.2-K electron concentration was $1.19 \times 10^{17}$ $cm^{-3}$. The sample was then annealed in vacuum to an electron concentration of $5.89 \times 10^{16}$ $cm^{-3}$ and finally in Hg vapor to a concentration of $2.84 \times 10^{17}$ $cm^{-3}$. The mobilities following the annealing steps are shown in Fig. 13 as functions of temperature from 4.2 to 300 K. The theoretical curves shown in Fig. 13 were obtained by adjusting the strength of the neutral scattering mechanism to match the 4.2-K mobility of the as-grown ($n_e = 1.19 \times 10^{17}$ $cm^{-3}$) sample. The scattering introduced corresponded, for example, to that from $10^{19}$ $cm^{-3}$ neutral centers with 2.5-eV potential wells extending over a sphere with radius equal to one lattice constant. These numbers are not to be taken too seriously for there are an infinite number of combinations which yield the same scattering strength. We emphasize that the neutral scattering strength was chosen to fit the 4.2-K mobility of the as-grown sample, and no further adjustments were made to fit the mobilities of the annealed samples. Only the donor concentrations were changed, being set equal to the 4.2-K electron concentrations. The agreement between the observed and calculated mobilities is better

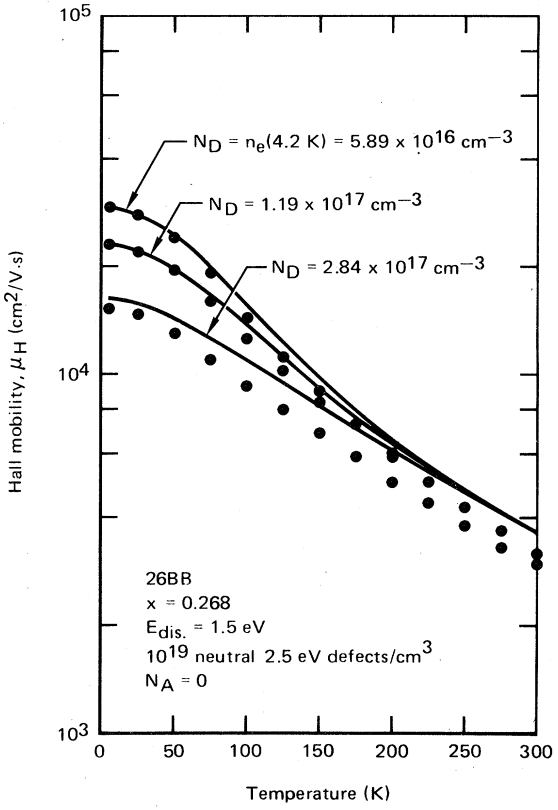


FIG. 13 Hall mobilities as functions of temperature of sample 26*BB* with $x = 0.268$ in the as-grown condition [$n_e$ (4.2 K) = $1.19 \times 10^{17}$cm$^{-3}$], after vacuum anneal [$n_e$ (4.2 K) = $5.89 \times 10^{16}$ cm$^{-3}$], and after Hg anneal [$n_e$ (4.2 K) = $2.84 \times 10^{17}$ cm$^{-3}$]. The theoretical curves for $\mu_H$ were calculated with the low fit for $\epsilon_\infty$ (curve 2 of Fig. 4) and the value of 1.5 eV for the disorder potential $E_{dis}$. The sample was assumed to be uncompensated with $N_D = n_e$ (4.2 K) and with $10^{19}$ cm$^{-3}$ neutral 2.5-eV defects which were unaffected by the annealing.

than 6% at low temperatures. At 300 K the observed mobilities of the two low-concentration samples are 11% less than the calculated values, while the high-concentration sample's observed mobility lies 16% below the theory.

Obviously no firm conclusions about the scattering mechanisms operative in the low mobility samples can be made on the basis of such limited data. However, the preceding analysis is highly suggestive of the existence of a very stable electrically neutral native defect in the alloy system, particularly in the low-$x$ region. Such a defect has been suggested for HgSe on the basis of both electrical mobility[4] and thermal conductivity[32] studies, and it is reasonable to assume that if it is present in HgSe, it would also be present in the low-$x$ region of the $Hg_{1-x}Cd_xSe$ alloy system.

There is another possible explanation for the behavior of the low mobility samples which cannot be completely ruled out. For these samples, the mean-free path associated with the scattering from the neutral centers is of the order of 0.5 $\mu$m, and it varies by only about 20% with energy in the range important in conduction processes (from the band edge to $E_F$ at low temperatures and to $3k_BT$ above the edge at high temperatures). Thus, it is conceivable that some macroscopic crystalline imperfection on the scale of 0.1–1 $\mu$m could produce behavior similar to that calculated for neutral defect scattering. A microscopic examination of the sample surfaces produces no evidence for imperfections on this scale, but they cannot be completely ruled out.

We would have obtained nearly the same results had we ignored the data of Figs. 2 and 3 on the optical-phonon oscillator strengths and instead calculated the $F_i$ with the assumptions that HgSe and CdSe unit cells retain their endpoint $e_T^*$ values over the whole composition range and that the $N_i$ are given by

$$N_{HgSe} = (1-x)N_a \tag{66}$$

and

$$N_{CdSe} = xN_a\ . \tag{67}$$

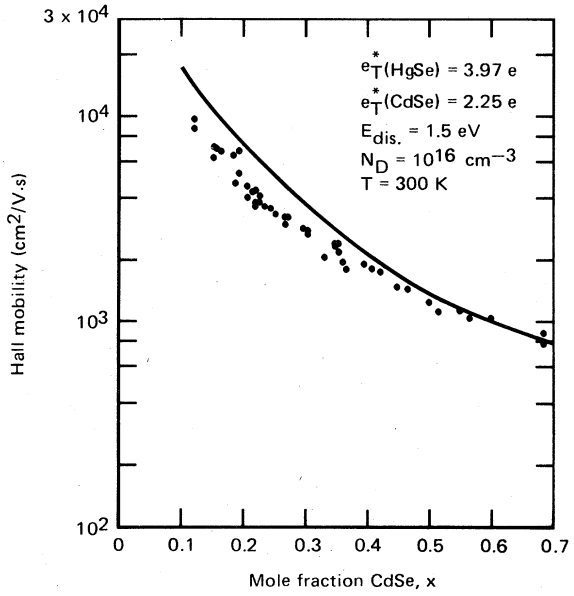


FIG. 14. 300-K Hall mobilities of $Hg_{1-x}Cd_xSe$ samples as functions of alloy composition. The theoretical curve was calculated with the high fit for $\epsilon_\infty$ (curve 1 of Fig. 4), a value of 1.5 eV for the disorder potential $E_{dis}$, and with the electron–LO-phonon coupling calculated from Eqs. (26), (66), and (67) under the assumption that HgSe and CdSe unit cells retain their endpoint $e_T^*$ values independent of alloy composition.

This calculation is shown for $T = 300$ K in Fig. 14, using[4,33] $e_T^*(\mathrm{HgSe}) = 3.95e$ and $e_T^*(\mathrm{CdSe}) = 2.25e$. Although the oscillator strengths do not obey such a simple linear dependence on $x$, the total scattering is nearly the same as if they did.

## IV. SUMMARY AND CONCLUSIONS

The picture of the intrinsic scattering processes in the $Hg_{1-x}Cd_xSe$ alloys which emerges from this study is very simple: the dominant scattering mechanism at room temperature, throughout the entire composition range studied, is LO-phonon scattering. This is to be expected because both HgSe and CdSe have rather high effective charges. Compositional-disorder scattering accounts for about 5% of the total scattering at $x = 0.12$ and about 21% at $x = 0.68$. The increase in relative importance of disorder scattering with increasing $x$ is due not only to the factor $x(1-x)$ in the scattering strength, but also to the increase of the electron effective mass and the decrease in strength of the electron-LO-phonon coupling. Acoustical-phonon scattering is relatively unimportant for all compositions and temperatures, and the hole concentrations, even at the highest temperature of this investigation, were too small for electron-hole scattering to be of significance.

The picture of the defect scattering processes, on the other hand, is very complex. There is evidence for four kinds of defects. Both HgSe and CdSe are characteristically $n$-type at all temperatures, and thus there are donors associated with native defects of both compounds in the alloy system. In addition, CdSe is typically highly compensated, and the low-temperature data above $x = 0.35$ are well accounted for by assuming partial compensation. Below $x = 0.3$ there are many samples with mobilities far below the theoretical values even at room temperature, and both the temperature dependence and low-temperature electron-concentration dependence of the mobilities of these samples are well explained by the addition of scattering by a stable neutral defect. A neutral defect has been suggested for HgSe on the basis of both thermal conductivity and low-temperature electron-mobility studies.

With the exception of the donor associated with HgSe, hardly anything is known about these defects. Because annealing in Hg vapor always effects an increase in electron concentration, the HgSe donor is believed to be associated with a stoichiometric excess of Hg in the lattice and may be a Hg interstitial. The apparent decrease in electron concentration and low-temperature mobility of the high-$x$ samples upon prolonged exposure to air suggests that the acceptor associated with CdSe may be oxygen. Further studies of the relation between the electrical transport properties and the growth and annealing conditions would be helpful for identifying these defects.

## ACKNOWLEDGMENTS

Supported by Office of Naval Research Contract No. N00014-74-C-0318, Air Force Materials Laboratory Director's Funds Contract No. F33615-74-C-5167, and by the McDonnell Douglas Corporation Independent Research and Development Program.

## APPENDIX

The functions appearing in the LO-phonon scattering operator $\mathcal{L}_{\mathrm{LO}}$ are defined as follows:

$$R_\pm(y,\theta) = F_\lambda(y)F_\lambda(y\pm\theta)(s_\pm^2+s^2)\sum_{n=0}^{2}\rho_n^\pm(y,\theta)V_{n+1}^\pm(y,\theta)\,, \tag{A1}$$

$$S_\pm(y,\theta) = F_\lambda(y)F_\lambda(y\pm\theta)s^2(s_\pm^2+s^2)\sum_{n=0}^{2}\rho_n^\pm(y,\theta)V_n^\pm(y,\theta)\,, \tag{A2}$$

$$F_\lambda(y) = \frac{3[2\delta^2\beta^3y^3+\delta(3-\delta)\beta^2y^2+\frac{4}{3}(1-\delta)\beta y-\frac{2}{3}]}{2(\frac{3}{2}\delta\beta y+1)^2}\,, \tag{A3}$$

$$b_1 = [\sqrt{2}/3N(\beta y)][(\tfrac{3}{2}\delta\beta y+1)/\beta y(\delta\beta y+1)]^{1/2}\,, \tag{A4}$$

$$c_1 = [(\delta\beta y+\tfrac{2}{3})/N(\beta y)][(\tfrac{3}{2}\delta\beta y+1)/\beta y(\delta\beta y+1)]^{1/2}\,, \tag{A5}$$

$$\rho_0^\pm(y,\theta) = (aa_\pm)^2 - bb_\pm[(bc_\pm+cb_\pm)/\sqrt{2}] + \tfrac{1}{2}(bc_\pm+cb_\pm)^2+\tfrac{1}{4}(bb_\pm)^2\,, \tag{A6}$$

$$\rho_1^\pm(y,\theta) = 2aa_\pm(b_1b_{1\pm}+c_1c_{1\pm})\,, \tag{A7}$$

$$\rho_2^\pm(y,\theta) = \tfrac{3}{4}(b_1b_{1\pm})^2 + b_1b_{1\pm}[(b_1c_{1\pm}+c_1b_{1\pm})/\sqrt{2}] + 2b_1b_{1\pm}c_1c_{1\pm} - \tfrac{1}{2}(b_1c_{1\pm}+c_1b_{1\pm})^2+(c_1c_{1\pm})^2\,, \tag{A8}$$

$$V_0^\pm(y,\theta) = -\frac{1}{q_\pm}\left(\frac{2g_\infty^2r_\pm}{p_\pm^2-4r_\pm^2}+\frac{1}{2}\ln\left|\frac{p_\pm-2r_\pm}{p_\pm+2r_\pm}\right|\right)\,, \tag{A9}$$

$$V_1^\pm(y,\theta) = r_\pm\left(\frac{p_\pm}{p_\pm^2-4r_\pm^2}-\frac{1}{q_\pm}-\frac{p_\pm^2}{q_\pm(p_\pm^2-4r_\pm^2)}\right) + \frac{1}{4}\left(1-\frac{2p_\pm}{q_\pm}\right)\ln\left|\frac{p_\pm-2r_\pm}{p_\pm+2r_\pm}\right|\,, \tag{A10}$$

$$V_2^\pm(y,\theta) = \frac{1}{4}\left\{r_\pm\left[1-\frac{2p_\pm}{q_\pm}+\left(1-\frac{p_\pm}{q_\pm}\right)\frac{p_\pm^2}{p_\pm^2-4r_\pm^2}\right] + \frac{p_\pm}{2}\left(2-\frac{3p_\pm}{q_\pm}\right)\ln\left|\frac{p_\pm-2r_\pm}{p_\pm+2r_\pm}\right|\right\}\,, \tag{A11}$$

$$V_3^{\pm}(y,\theta) = -\frac{r_{\pm}^3}{3q_{\pm}} + \frac{p_{\pm}r_{\pm}}{2}\left(1 - \frac{3p^{\pm}}{2q_{\pm}} + \frac{p_{\pm}^2}{2(p_{\pm}^2 - 4r_{\pm}^2)} - \frac{p_{\pm}^3}{2q_{\pm}(p_{\pm}^2 - 4r_{\pm}^2)}\right) + \frac{p_{\pm}^2}{16}\left(3 - \frac{4p_{\pm}}{q_{\pm}}\right)\ln\left|\frac{p_{\pm} - 2r_{\pm}}{p_{\pm} + 2r_{\pm}}\right|, \quad \text{(A12)}$$

$$q_{\pm} = s_{\pm}^2 + s^2, \quad \text{(A13)}$$

$$p_{\pm} = q_{\pm} + g_{\infty}^2, \quad \text{(A14)}$$

$$r_{\pm} = ss_{\pm}, \quad \text{(A15)}$$

$$g_{\infty}^2 = \frac{\hbar^2}{2\mu' m_0 E_g \epsilon_{\infty}}\left[(k_{\mathrm{FT}}^{e})^2 + (k_{\mathrm{FT}}^{\mathrm{lh}})^2\right]. \quad \text{(A16)}$$

In the above, $R_-$ and $S_-$ are zero for $y - \theta - \beta^{-1} < 0$. The definitions of the $\rho_i$ are slightly changed from the usual definitions[4,24] to speed numerical computation by avoiding 0/0 convergence problems near the band edge.


*Present address: Honeywell Radiation Center, Lexington, Mass. 02173.

[1]T. C. Harman and A. J. Strauss, J. Apl. Phys. 32, 2265 (1961).

[2]C. R. Whitsett, Phys. Rev. 138, A829 (1965).

[3]J. G. Broerman, Phys. Rev. B 2, 1818 (1970).

[4]S. L. Lehoczky, J. G. Broerman, D. A. Nelson, and C. R. Whitsett, Phys. Rev. B 9, 1598 (1974).

[5]R. G. Wheeler and J. O. Dimmick, Phys. Rev. 125, 1805 (1962).

[6]A. Kalb and V. Leute, Phys. Status Solidi 5, K199 (1971).

[7]D. A. Nelson, C. J. Summers, and C. R. Whitsett, J. Electron Mater. 6, 507 (1977).

[8]J. Stankiewicz, W. Giriat, and W. Dobrowski, Phys. Status Solidi B 61, 267 (1974).

[9]I. N. Borisov, P. S. Kiriev, V. V. Mikhailin, and V. M. Bezborodova, Fiz. Tekh. Poluprov. 5, 829 (1971) [Sov. Phys.-Semiconduct. 5, 734 (1971)].

[10]P. S. Kiriev and V. V. Volkov, Fiz. Tekh. Poluprov. 7, 1419 (1973) [Sov. Phys.-Semiconduct. 7, 949 (1974)].

[11]P. A. Slodowy and W. Giriat, Phys. Status Solidi 48, 463 (1971).

[12]C. J. Summers, D. A. Nelson, C. R. Whitsett, and J. G. Broerman (unpublished).

[13]C. J. Summers, A. K. Bhatnager, and D. A. Nelson (unpublished).

[14]E. Cruceanu and S. Ionescu-Bujor, J. Mater. Sci. 4, 570 (1969).

[15]R. J. Iwanowski and T. Dietl, Phys. Status Solidi B 75, K83 (1976).

[16]E. O. Kane, J. Phys. Chem. Solids 1, 249 (1957).

[17]J. G. Broerman, *Proceedings of the Eleventh International Conference on the Physics of Semiconductors* (Polish Scientific, Warsaw, 1972), Vol. 2, p. 917.

[18]C. R. Whitsett and D. A. Nelson, J. Crystal Growth 6, 26 (1969).

[19]L. J. van der Pauw, Philips Res. Rep. 13, 1 (1958).

[20]G. A. Somorjai, J. Phys. Chem. Solids 24, 175 (1963).

[21]D. G. Seiler, R. R. Galazka, and W. M. Becker, Phys. Rev. B 3, 4274 (1971).

[22]M. Cardona, J. Phys. Chem. Solids 24, 1543 (1963).

[23]H. Ehrenreich, J. Phys. Chem. Solids 2, 131 (1957).

[24]J. G. Broerman, L. Liu, and K. N. Pathak, Phys. Rev. B 4, 664 (1971).

[25]W. Zawadzki and W. Szymânska, Phys. Status Solidi 45, 415 (1971).

[26]S. L. Lehoczky, D. A. Nelson, and C. R. Whitsett, Phys. Rev. 188, 1069 (1969).

[27]I. D. Zook, Phys. Rev. 136, A869 (1964).

[28]A. Jedrzejczak and T. Dietl, Phys. Status Solidi B 76, 737 (1976).

[29]D. L. Rode, Phys. Rev. B 2, 4036 (1970).

[30]L. Makowski and M. Glicksman, J. Phys. Chem. Solids 34, 487 (1973).

[31]M. Kohler, Z. Phys. 125, 679 (1949).

[32]C. R. Whitsett, D. A. Nelson, J. G. Broerman, and E. C. Paxhia, Phys. Rev. B 7, 4625 (1973).

[33]M. Balkanski, *Proceedings of the 1967 Conference on II VI Compounds*, edited by D. G. Thomas (W. A. Benjamin, New York, 1968), p. 1007.